Early moment-rate growth scales with rupture velocity during laboratory earthquakes

F. Arzu[1], B. Fryer[1], F. Paglialunga[1], C. Twardzik[1], Y. Xie[2], J.-P. Ampuero[1], F. Passelègue[1]

[1]Université Côte d'Azur, CNRS, Observatoire de la Côte d'Azur, Géoazur
[2]Institute of Geology and Geophysics, Chinese Academy of Sciences

Key Points:

- We measured moment-rate growth during laboratory earthquakes under controlled experimental conditions.
- Early moment-rate growth correlates with the initial rupture velocity, but not with final size.
- Final rupture-size information emerges only after substantial rupture growth, limiting early predictability.

Corresponding author: Arzu, F., `feyza.arzu@geoazur.unice.fr`

Abstract

Final size predictability of an ongoing rupture remains a fundamental question in earthquake physics. If small and large earthquakes differ during their earliest stages, information contained in the initial growth of moment rate functions (MRFs) could improve earthquake early warning. Testing this hypothesis with natural earthquakes is challenging because variations in tectonic setting, data coverage, and analysis methods can bias inferred MRFs. To overcome these limitations, we built a laboratory earthquake catalog and computed MRFs using two independent approaches: digital image correlation and quasi-static slip inversion. In our laboratory earthquake catalog, we find no systematic relationship between the initial MRF slope and final rupture length or seismic moment. Instead, the initial MRF slope scales with the initial rupture velocity. This result indicates that the early MRF growth reflects initial rupture dynamics rather than final rupture size, limiting its usefulness for earthquake-magnitude predictability.

Plain Language Summary

Whether the initiation of an earthquake reveals its final size remains an open question. If small and large earthquakes can be distinguished during their earliest stages, observable differences in their initial growth could improve earthquake early warning systems. Testing this hypothesis using natural earthquake catalogs is challenging because variations in data coverage, tectonic setting, and analysis methods can all affect observations. To minimize these sources of variability, we created a laboratory earthquake catalog using an experimental apparatus that produced a wide range of rupture lengths. We estimate moment rate functions (MRFs), which describe how seismic moment is released during rupture, using two independent approaches: digital image correlation using a high-speed camera and quasi-static slip inversion of near-field accelerometer data. Our results show that the initial MRF slope is not related to the final rupture size but is strongly correlated with the initial rupture velocity. This suggests that the final size of an earthquake is not controlled primarily by how rupture starts, but more by how rupture evolves as it propagates along the fault.

1 Introduction

Earthquakes are one of the most destructive natural hazards. While we cannot predict where and when the next earthquake will occur, earthquake early warning (EEW) systems can rapidly detect ongoing ruptures and provide alerts before strong ground shaking reaches populated areas (Allen & Kanamori, 2003). A fundamental question relevant for the speed and reliability of EEW is whether the initiation stage of an earthquake rupture contains information useful to quickly estimate its final size. This issue has been debated for decades. If rupture initiation does not carry information about the stress distribution and structural heterogeneity along the entire fault plane, which affects rupture propagation and arrest (i.e., Husseini et al. (1975); Okubo & Dieterich (1984); Bayart et al. (2016, 2018); Ke et al. (2018); Fryer et al. (2024); Paglialunga et al. (2026)), it is inherently difficult to determine the final size of the earthquake before rupture completion. Several studies suggest weak to moderate predictability of final rupture size from early earthquake characteristics (weak and moderate as defined in Meier et al. (2020)), including reports that small and large earthquakes can be distinguished by analyzing moment rate functions (MRFs) (Melgar & Hayes, 2019; Danré et al., 2019; Zeng et al., 2025), early ground motion parameters (Colombelli et al., 2014, 2020; Longobardi et al., 2025), and waveform onset characteristics (Ellsworth & Beroza, 1995; Zollo et al., 2006; Wang et al., 2022; Morad et al., 2025). In contrast, other studies argue against such predictability, emphasizing the apparent similarity of rupture initiation across a wide range of earthquake magnitudes (Meier et al., 2016, 2017, 2020; Trugman et al., 2019; Ide, 2019; Münchmeyer et al., 2022).

Assessing whether rupture initiation of natural earthquakes contains information about their final size is challenging because each earthquake is recorded under different conditions. Differences in tectonic setting, focal depth, fault geometry, and data coverage can strongly influence the inferred rupture properties. To reduce these sources of variability, several studies have applied strict event-selection criteria. For example, Ide (2019) excluded earthquakes deeper than 70 km and offshore events from their subduction-zone catalog. Likewise, Meier et al. (2017) focused exclusively on subduction-zone earthquakes, whereas Longobardi et al. (2025) retained only events with sufficient station coverage within a 25 km distance from the nearest receiver. Methodological differences in the estimation of MRFs may introduce additional biases. To account for this, Melgar & Hayes (2019); Meier et al. (2016); Münchmeyer et al. (2022) compared independent MRF catalogs derived using different methodologies (Vallée & Douet, 2016; Ye et al., 2016; Hayes, 2017). Although such selection criteria and methodological choices are necessary, each carries their own limitations and may introduce observational biases.

Laboratory experiments can address the aforementioned limitations by providing controlled and repeatable conditions, including identical receiver distributions and well-constrained fault geometry. They eliminate many of the biases when comparing different natural earthquakes, enabling a more direct investigation of the relationship between rupture initiation and final earthquake size. Although laboratory experiments and numerical models have been widely used to study rupture initiation, particularly the nucleation phase and the transition to dynamic propagation (Ohnaka, 2004; McLaskey & Lockner, 2014; Latour et al., 2013; Kaneko et al., 2016; McLaskey, 2019; Gori et al., 2021; Fryer et al., 2026), relatively few studies have examined whether the initiation process contains information about the eventual size of the rupture (Morad et al., 2025; Kiss et al., 2026; Pardo et al., 2026).

In this study, we construct an earthquake dataset of strike-slip-like laboratory earthquakes using a biaxial apparatus, and derive MRFs using two independent approaches: Digital Image Correlation and quasi-static slip inversion of near-field accelerometer data (Arzu et al., 2025). We use these two independent MRF catalogs to investigate whether the initial growth of MRFs contains information about final rupture size.

2 Experimental protocol

2.1 Experimental fault

Experiments were conducted using the biaxial apparatus *Crackdyn* at the Géoazur laboratory (Valbonne, France). The experimental fault is the interface between two polymethyl methacrylate (PMMA) blocks ($40 \times 10 \times 1$ cm^3 and $45 \times 10 \times 1.8$ cm^3), defining a planar fault surface of 40×1 cm^2 (Figure S1a). Normal loading was applied using three independently controlled vertical pistons, while shear loading was imposed by a horizontal piston. All pistons were instrumented with load cells sampled at 500 Hz. Normal load was manually adjusted using Enerpac hydraulic pumps, with target pressures ranging from 100 to 250 bar, depending on the experiment. Once the target normal load was reached, shear loading was applied using a PMHP 35-1000 hydraulic pump. The injection flow rate was fixed at 0.5 cm^3·min^{-1}. The reported normal pressure corresponds to the hydraulic gauge reading and does not directly represent the normal stress on the fault.

Dynamic rupture propagation was imaged using a Phantom TMX 6410 high-speed camera operating at 100 kHz, with a spatial resolution of 32×1280 pixels (pixel size ≈ 0.3 mm). The camera was triggered via an oscilloscope connected to a piezoelectric (acoustic) sensor glued on the sample close to the fault interface (Figure S1a). In addition, both plates were coated on the camera side with a speckle pattern to enable Digital Image Correlation (DIC) during the nucleation and propagation stages of the frictional ruptures. This setup provides direct spatiotemporal measurements of fault slip during the entire propagation of the rupture front. The characteristic speckle size was ~ 0.6–1 mm ($\sim$ 2–3 pixels), ensuring sufficient contrast for robust image correlation. The fault was illuminated by four high-intensity light sources: three positioned in front of the sample to illuminate the speckle pattern, and one polarized-light source located behind the apparatus. This configuration enabled simultaneous DIC and photoelastic imaging of stress changes in the birefringent PMMA, allowing us to track rupture propagation (Rosakis et al., 1999; Nielsen et al., 2010).

To control the nucleation location during the experiments, a Teflon patch was placed on one side of the fault. Patch dimensions were either 5×1 or 10×1 cm^2, depending on the experiment. Due to their low friction, these patches promote creep and concentrate stress at their edge, leading to systematic rupture initiation at this location. The Teflon region appears as a darker area on the left side of the fault in Figure S1a due to reduced light transmission.

Finally, the fault was instrumented with 20 Brüel & Kjær type 8309 accelerometers (corner frequency 56 kHz), continuously sampled at 2 MHz. Sensors are individually calibrated, allowing direct conversion from voltage to particle acceleration. They were oriented parallel to the fault and positioned at distances of 2 and 4 cm to record near-field fault-parallel acceleration (Figure S2).

2.2 Methods

We construct MRF catalogs using two independent approaches. First, we apply DIC to high-speed optical images of the fault interface to obtain a direct observation of the spatio-temporal distributions of fault slip, $\delta(x,t)$, and slip rate, $\dot{\delta}(x,t)$. Second, we estimate $\delta(x,t)$ and $\dot{\delta}(x,t)$ by inverting near-field accelerometer recordings using a quasi-static slip inversion scheme (Arzu et al., 2025). This second method provides an indirect estimate of the fault-slip evolution and is conceptually closer to the approaches used to study natural earthquakes. For both datasets, MRFs are obtained by computing the spatial average of slip-rate along the fault, $\dot{\bar{\delta}}(t)$, and then

$$\dot{M}_0(t) = \mu A \, \dot{\bar{\delta}}(t), \tag{1}$$

where μ is the shear modulus and A is the imaged fault area. Additional processing steps and methodological details are provided in the Supplementary Information.

The final rupture length is measured from videograms, like the one shown by background colors in Figure 1a (from brown to green), that represent variations in transmitted light intensity related to shear stress changes along the fault (Latour et al., 2024). A horizontal line of pixels located close to the fault was extracted for 1-D spatial analysis. The average light intensity over the first 20 frames was used as a reference. As the rupture propagates, evolving stress states modify the pixel intensities, which are compared to the reference image to construct the videogram and visualize the rupture propagation. This measurement of final rupture length is independent of both the DIC and inversion analyses.

3 Results

3.1 Representative event

Figure 1 shows a representative event performed using a Teflon patch extending from $x = 0$ to $x = 10$ cm. The rupture nucleates near $x = 10$ cm, propagates to the right, and arrests near $x = 20$ cm after ~ 0.4 ms, corresponding to a rupture velocity of approximately half the S-wave speed (i.e. dashed line in Figure 1a). Rupture growth toward the left, within the Teflon patch, is limited and remains minor throughout the

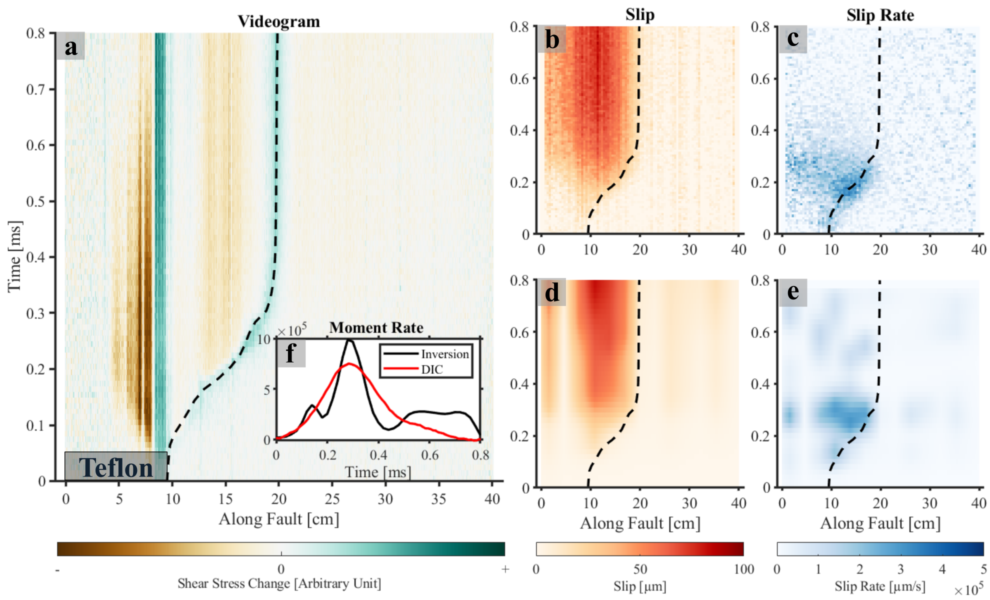

Figure 1. Verification of slip Inversion and DIC techniques. (a) Photoelasticity, proportional to shear stress change, is shown in the background. Green indicates an increase in shear stress, while brown indicates a decrease. A 10 cm Teflon patch is placed $x = 0$ cm to $x = 10$ cm along the fault. The dashed line denotes the manually picked (smoothed) rupture front in (a-e). (b, d) Red colorscale represents the spatio-temporal slip distribution along the fault obtained from DIC and inversion, respectively. (c, e) Blue colorscale represents the corresponding spatio-temporal slip rate distributions from DIC and inversion, respectively. (f) Corresponding MRFs. For the inversion results, time zero corresponds to the earliest P-wave arrival at the accelerometers; whereas for the videogram and DIC, it corresponds to the rupture initiation time.

catalog. Therefore, we only consider the rightward rupture front. We estimate the final rupture length from the maximum extent of the rightward rupture front.

3.2 Method comparison: DIC versus inversion

We illustrate the two independent approaches to estimate the spatio-temporal evolution of slip applied to the representative event in Figure 1. The rupture front in Figure 1a, is superimposed on the distributions of slip and slip rate obtained from DIC and inversion (Figure 1b–e).

The DIC results reveal a close match between rupture propagation and fault slip evolution. Slip accumulates behind the rupture front (Figure 1b), whereas the slip rate is strongly localized near the propagating front (Figure 1c). The highest slip-rate amplitudes are observed where the rupture front is steepest, indicating the largest rupture velocity. As the rupture decelerates and eventually arrests near $x \approx 20$ cm at ~ 0.4 ms, slip rates progressively decrease and vanish across the fault, while slip reaches its final distribution. Some slip occurs within the Teflon patch, consistent with the videogram.

The inversion results exhibit the same first-order features (Figure 1d and 1e). The rupture initiation point, the rupture propagation, and the arrest location are all consistent with the videogram and the DIC measurements. As with the DIC results, the highest slip rates occur during the phase of fastest rupture propagation, and slip rate am-

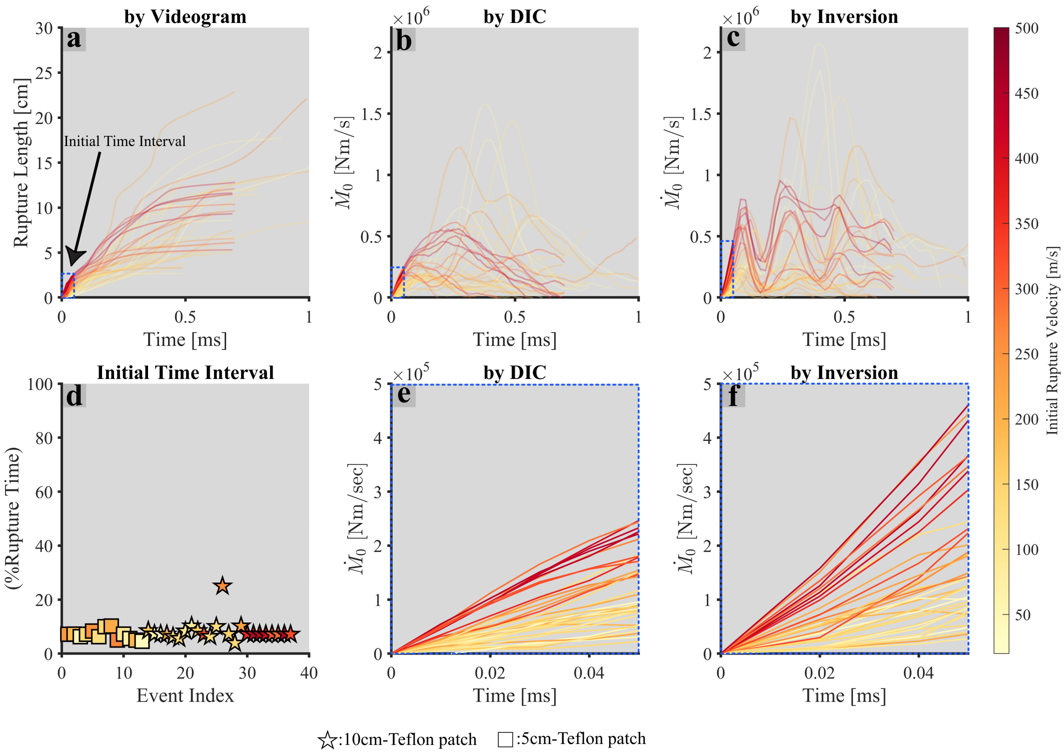

Figure 2. Rupture evolution and MRFs for the full catalog. (a) Rupture length evolution for all events. The blue dashed rectangle (also in other panels) indicates the initial time window, defined as the first 0.05 ms of rupture. Colors indicate the average rupture velocity within this window. (b, c) Catalog of MRFs obtained from DIC and inversion, respectively. Time is relative to rupture initiation for DIC and to the earliest signal arrival at the accelerometers for inversion. (d) Ratio of initial window duration to rupture duration. For most events, the initial window is less than 10% of the rupture duration. Squares and stars denote events nucleating near x=5 cm and x=10 cm along the fault, respectively, corresponding to the Teflon patch location. (e, f) Zoomed-in views of (b) and (c) over the initial time window.

plitudes decrease once the rupture slows down. Differences between the two methods are mainly expressed in the spatial and temporal smoothness of the inferred slip-rate field, which reflects the parameterization used for the inversion. The resulting MRFs (Figure 1f) are broadly consistent between the two approaches, capturing the timing of rupture growth and arrest. Although the inverted MRF exhibits additional secondary peaks, these do not affect the overall evolution of moment release and are discussed in more detail in the following section.

3.3 Catalog-scale rupture behavior and MRFs

We analyse the 37 events in our dataset using both DIC and quasi-static inversion of off-fault sensors. For 13 of the 37 events, rupture initiates around $x = 5$ cm, while for the remaining 24 events, rupture nucleates around $x = 10$ cm, depending on Teflon patch size. To avoid artificial effects of the sample boundaries, we restrict the analysis to self-arrested events, that is, events that stop before reaching the fault edge.

Figure 2a shows the temporal evolution of rupture length for all self-arrested events. Final rupture lengths ranged from 3 to 23 cm, and peak rupture velocities ranged between 184 and 1051 m/s, corresponding to 14% and 78% of the S-wave speed (See Figure S6a). We observe different rupture evolution styles across the catalog: some events exhibit a single acceleration phase followed by arrest, whereas others show several acceleration and deceleration phases.

Figures 2(b,c) show the MRFs obtained from DIC and inversion, respectively. Both capture the rupture complexity observed in Figure 2a. However, the MRFs obtained from the quasi-static inversions exhibit systematic oscillations, likely associated with S-waves reflected by the sample boundaries and recorded by the accelerometers, but not accounted for by the static Green's functions used in our inversions. Because the ruptures are slower than the S-wave speed in our experiments, S-waves are recorded prior to rupture arrest. Reflections from the top boundary of the upper block, located 10 cm from the fault, introduce a characteristic timescale of $20\text{cm}/1345\text{m/s} \approx 0.15$ ms, consistent with the observed oscillation period in the inverted MRFs. To avoid this artifact, the initial time windows for the predictability analysis based on the inverted MRFs (Figure 2(c,f)) must be shorter than 0.15 ms.

3.4 Initial MRF slope versus rupture properties

To identify the physical parameters controlling the initial MRF growth, we first examine whether the initial MRF slope is related to the final rupture size. Here, the initial slope is calculated as the average slope of the MRFs over an initial time window comprising the first 0.05 ms of rupture (Figure 2(e,f)). For most events, this time window represents less than 10 percent of the total rupture duration (Figure 2d), satisfying the strong predictability criterion proposed by Meier et al. (2020). The initial MRF slope is then compared with the final rupture length of each event (Figure 3(a,b)).

No systematic relationship is observed between the initial MRF slope and the final rupture length, regardless of whether the MRF is estimated from DIC or from quasi-static inversion (Figure 3(a,b)). We find that events with similar rupture lengths span nearly the entire range of observed MRF slopes. For example, ruptures reaching approximately 10 cm exhibit initial slopes ranging from less than 0.5×10^9 Nm/s^2 to more than 4×10^9 Nm/s^2. Similarly, events with similar initial MRF slopes can reach different rupture lengths. The absence of any clear trend is further supported by the distribution of final seismic moments obtained from the DIC (colors in Figure 3), which shows no systematic variation with respect to the initial MRF slope.

To investigate whether information about the final size of the rupture emerges later during rupture growth, we repeat the analysis using progressively larger time windows to compute the initial MRF slope. When the initial time window is extended to 0.2 ms (moderate predictability criterion), corresponding to approximately 20-40 percent of the rupture duration for most events (Figure S7), the inversion results still show no systematic relationship between initial MRF slopes and rupture length (likely because the acceleration records are already influenced by reflected S-waves), whereas the measurements from the DIC start to display two partially separated populations (Figure S10). Extending the initial time window further to 0.3 ms (weak predictability criterion), corresponding to approximately 30-60 percent of the rupture duration for most events (Figure S8), strengthens this apparent trend in the DIC catalog (Figure S11), with larger ruptures tending to exhibit steeper initial MRF growth. However, at this stage, the rupture has already propagated over a substantial fraction of its final extent, and the MRF has approached or exceeded its peak amplitude for many events (Figs. S8 and S9). Consequently, although information about final rupture size may progressively emerge as the rupture develops, it is not the case during the earliest stages of rupture propagation and therefore has limited relevance for EEW applications.

If the initial MRF slope does not reflect the final rupture size, what is its controlling factor? Both the DIC and inversion catalogs show a clear relationship between the

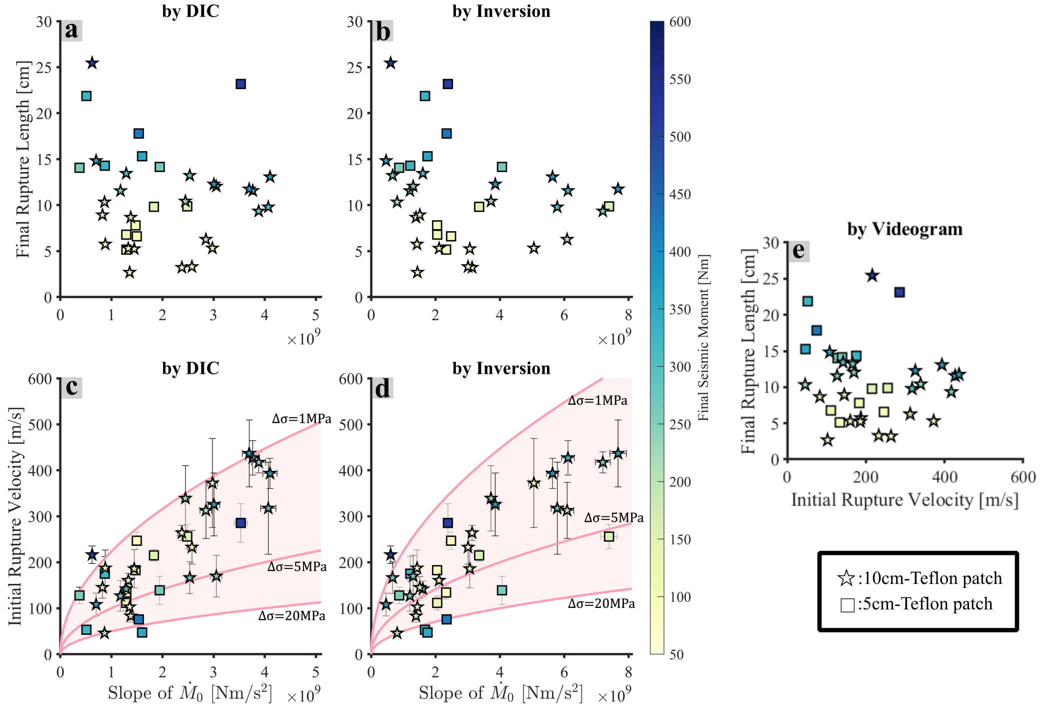

Figure 3. (a, b) Relationship between final rupture length and the initial slope of the MRF (initial time window of 0.05 ms), derived from DIC and inversion methods, respectively. (c, d) Relationship between the initial average rupture velocity and the initial MRF slope, also obtained from DIC and inversion, respectively. Pink curves represent theoretical scaling relations under the assumptions of constant stress drop and constant rupture velocity, evaluated for different stress-drop values. The color scale indicates seismic moment estimated from DIC analysis. Horizontal and vertical bars represent the variability in the initial MRF slope and rupture velocity over the initial time windows. Here, the variability of both quantities within the selected time window is estimated as the standard deviation over subsets defined with 10 μs increments of the initial time window. Lastly, stars and squares denote events initiating at the edge of 5 cm and 10 cm long Teflon patches, respectively. (e) Direct comparison of the initial rupture velocity and final rupture length, obtained from the videogram.

initial MRF slope and the initial rupture velocity, both measured over the initial 0.05 ms (Figures 2(e,f) and 3(c,d)). Events characterized by steeper initial MRF growth systematically exhibit faster initial rupture propagation, whereas slowly propagating ruptures are associated with less steep initial MRF slopes. This robust relationship emerging through the entire catalog is also predicted by theoretical source models (Deichmann, 1997; Renou et al., 2019). Importantly, it remains observable when the analysis time window is extended (Figs. S11 and S12), even though the scatter progressively increases as rupture propagation becomes influenced by fault-scale heterogeneities and rupture arrest processes.

Our observations demonstrate a higher initial rupture velocity does not necessarily lead to a larger final rupture size (Figure 3e). For example, some of the initially-fastest ruptures in the catalog reach only moderate rupture lengths, while several larger ruptures initiate with comparatively modest rupture velocities and MRF slopes. Similarly, events exhibiting nearly identical initial rupture velocities can terminate at very different rupture lengths.

4 Discussion

Our laboratory observations show that the initial MRF slope is controlled by the initial rupture velocity and is not systematically related to the final rupture length nor the final seismic moment (Figure 3). Thus, in our experiments, the final rupture extent is not primarily determined by initial rupture dynamics, but by factors that emerge during later stages of rupture propagation.

Fracture mechanics offers a theoretical framework for understanding which factors control rupture velocity from initiation to termination. Theoretically, the rupture velocity, v_r, is controlled by the ratio of the static energy release rate, G_0, to the fracture energy, G_c, as (Freund, 1998),

$$v_r(L) \approx v_R \left(1 - \frac{G_c}{G_0(L)}\right), \tag{2}$$

where v_R is the Rayleigh-wave velocity and L is the crack length. The static energy release rate depends on the effective stress drop $\Delta\sigma$, which is a weighted average of stress drop along the rupture (Freund, 1998; Tada et al., 2000), as

$$G_0 \propto \frac{\Delta\sigma^2 L}{\mu}, \tag{3}$$

where μ is the shear modulus. During the initial stage of the rupture, G_0 and thus the initial rupture velocity are controlled by initial stresses around the nucleation region (Fryer et al., 2026). As the rupture grows, however, the contribution of the nucleation region to G_0 becomes weaker, and rupture velocity is increasingly influenced by the stress and frictional heterogeneities encountered far from the nucleation region.

The observed strong dependence of early MRF growth on initial rupture velocity (Figure 3(c,d)) can be explained theoretically, to the first order. For a unilateral rupture of length L, width W and uniform stress drop $\Delta\sigma$, the seismic moment scales as

$$M_0 \propto \Delta\sigma L^2 W. \tag{4}$$

Assuming a constant initial rupture velocity, v_r, the rupture length evolves initially as

$$L(t) = v_r t, \tag{5}$$

which yields

$$M_0(t) \propto \Delta\sigma v_r^2 t^2 W. \tag{6}$$

The moment acceleration, which is the initial MRF slope, scales with stress drop and with the square of the rupture velocity as

$$\ddot{M}_0(t) \propto 2\Delta\sigma v_r^2 W. \tag{7}$$

Moreover, combining Eqs. 2 and 3 indicates that v_r and $\Delta\sigma$ are theoretically expected to be positively correlated, as also observed in experimental studies (Passelègue et al., 2020). Accounting for the combined effects of v_r and $\Delta\sigma$, Eq. 7 is consistent with the trends observed in Figure 3(c,d): the data is consistent with the 1−20 MPa stress drop range considered reasonable for the loading conditions used in our biaxial experiments. As we extend the initial time window to 0.2 ms and 0.3 ms (Figures S10 and S11), the data exhibit a clearer trend concentrated within the 1−5 MPa range, in agreement with the static stress drop estimated from Eq. 4.

Our observation that the final rupture extent is not primarily determined by initial rupture velocity (Figure 3(e)) can be interpreted in the framework of fracture mechanics as due to a lack of spatial correlation in the state of stress and strength along the fault. Rupture arrests if it reaches an under-stressed region or a fracture energy barrier such that $G_0 < G_c$ (Kammer et al., 2015; Bayart et al., 2016, 2018; Ke et al., 2018). If heterogeneities of G_c/G_0 are uncorrelated at length scales larger than the nucleation length, the initial rupture speed and the final rupture size should not be correlated, in agreement with our experimental observations.

This interpretation raises an important question: why do some studies, both at natural (Nakatani et al., 2000; Longobardi et al., 2025) and laboratory scales (Morad et al., 2025), report a correlation between rupture initiation and final earthquake size?

A first possibility within the fracture mechanics framework is that the nucleation size remains independent of the final rupture size, while the initial stress varies from one event to another simultaneously along the whole fault. In this case, the available energy is spatially correlated, a larger G_0 within the nucleation region is accompanied by a larger G_0 along the rest of the fault, promoting both faster initial rupture and larger final rupture size. A positive correlation between initial rupture velocity and final rupture size would emerge, as reported in natural earthquake catalogs by Nakatani et al. (2000) and in a laboratory-scale catalog by Morad et al. (2025).

Indeed, Morad et al. (2025) reported that large ruptures accelerate faster than small ones for events that have relatively smooth initial stresses controlled only by the prescribed experimental loading/boundary conditions, but not for ruptures that propagate through highly heterogeneous (less spatially correlated) stress fields inherited from previous ruptures hat arrested within the sample. However, in some of our experiments (experiments #2, #6, and #8 in Figure S6), we do observe a correlation between initial MRF slope and final seismic moment (Figure S4), despite each event propagating through the fault prestressed by preceding ruptures. Our current observations do not allow us to determine the initial stress at the nucleation location. However, the strain gauges distributed along the fault (representative example shown in Figure S3c) indicate that both the local shear stress and stress drop increase along the fault for each successive event. These observations highlight the complexity of rupture predictability in heterogeneous stress environments, demonstrating that stress redistribution by previous arrested ruptures does not necessarily eliminate the apparent predictability of subsequent ruptures.

Morad et al. (2025) further note that, at the end of the predefined initial time window (30 µs corresponding to $15-20\%$ of the rupture duration), the rupture length is roughly $25-30$ mm, corresponding to an initial rupture velocity of $800-1000$ m/s. Even though we do not have such large initial rupture velocity values in our catalog, restricting our analysis to ruptures in our catalog with relatively fast initial rupture velocities (>250 m/s in Figure S5) reveals a positive correlation between initial moment acceleration and the seismic moment across the entire restricted catalog. We propose that the differences in rupture predictability observed in initially slow and fast events might arise from the relative contributions to the fault stress of two factors: the prescribed loading and the residual stresses left by previous ruptures. The former affects the whole fault, whereas the latter only affects areas beyond the nucleation region where previous ruptures stopped. Ruptures that start faster necessarily have a high stress around the nucleation region, thus they are associated with larger loading stresses, thus a weaker contribution from residual stress. The loading stress being spatially correlated, these initially fast ruptures tend to be more predictable. In contrast, ruptures that start slow have a relatively weaker contribution from the loading stresses, a more heterogeneous initial stress controlled by the residual stress, thus are less predictable.

A second possibility is that larger earthquakes are associated with larger nucleation lengths. In that case, larger ruptures would start slower since Eq. 2 can also be written as $v_r(l) \approx v_s \left(1 - \frac{l_\infty}{l}\right)$, where l_∞ denotes the limiting nucleation length scale (Rubin & Ampuero, 2005). This would produce a weaker initial impulse for larger earthquakes, as reported by Beroza & Ellsworth (1996); Colombelli et al. (2020); Longobardi et al. (2025). However, there is currently no strong theoretical basis for expecting nucleation length to systematically scale with final rupture size. Nevertheless, such a relationship cannot be excluded in natural earthquake catalogs.

These two possibilities may help reconcile apparently contradictory observations in the literature; such as Nakatani et al. (2000) reporting that larger earthquakes tend to exhibit steeper initial growth, whereas Longobardi et al. (2025) reported the opposite trend. Our observations suggest that whether a correlation between MRF growth and final earthquake size emerges depends on how nucleation properties and stress conditions are interrelated within a given earthquake catalog. Understanding these relationships may be key to reconciling the contrasting observations reported in both laboratory and natural earthquake studies.

Acknowledgments

F.A., B.F., and F.X.P. acknowledge support from the European Union (ERC Starting Grant HOPE number 101041966). F.P. acknowledges support from the SNF PostDoc.Mobility grant P500PN_222262. J.P.A. was supported by the French government through the UCA-JEDI Investments in the Future project (ANR-15-IDEX-01) managed by the National Research Agency (ANR). F.A. thanks Martijn van den Ende for the helpful discussion.

5 Availability Statement

The data used in this study is not publicly available at the time of submission, but will be make openly available on Zenodo upon acceptance of the manuscript.

References

Allen, R. M., & Kanamori, H. (2003). The potential for earthquake early warning in southern california. *Science*, *300*(5620), 786-789. Retrieved from https://www.science.org/doi/abs/10.1126/science.1080912 doi: 10.1126/science.1080912

Arzu, F., Twardzik, C., Fryer, B., Xie, Y., Ampuero, J. P., & Passelègue, F. (2025, 12). Static and quasi-static inversion of fault slip during laboratory earthquakes. *Geophysical Journal International*, *244*(2), ggaf507. doi: 10.1093/gji/ggaf507

Bayart, E., Svetlizky, I., & Fineberg, J. (2016). Fracture mechanics determine the lengths of interface ruptures that mediate frictional motion. *Nature Physics*, *12*(2), 166–170.

Bayart, E., Svetlizky, I., & Fineberg, J. (2018). Rupture dynamics of heterogeneous frictional interfaces. *Journal of Geophysical Research: Solid Earth*, *123*(5), 3828–3848.

Beroza, G. C., & Ellsworth, W. L. (1996). Properties of the seismic nucleation phase. *Tectonophysics*, *261*(1-3), 209–227. Retrieved 2026-04-07, from https://linkinghub.elsevier.com/retrieve/pii/0040195196000674 doi: 10.1016/0040-1951(96)00067-4

Colombelli, S., Festa, G., & Zollo, A. (2020, 10). Early rupture signals predict the final earthquake size. *Geophysical Journal International*, *223*(1), 692-706. Retrieved from https://doi.org/10.1093/gji/ggaa343 doi: 10.1093/gji/ggaa343

Colombelli, S., Zollo, A., Festa, G., & Picozzi, M. (2014, June). Evidence for a difference in rupture initiation between small and large earthquakes. *Nature Communications*, *5*(1), 3958. Retrieved from https://doi.org/10.1038/ncomms4958 doi: 10.1038/ncomms4958

Danré, P., Yin, J., Lipovsky, B. P., & Denolle, M. A. (2019). Earthquakes within earthquakes: Patterns in rupture complexity. *Geophysical Research Letters*, *46*(13), 7352-7360. doi: https://doi.org/10.1029/2019GL083093

Deichmann, N. (1997). Far-field pulse shapes from circular sources with variable rupture velocities. *Bulletin of the Seismological Society of America*, *87*(5), 1288–1296. Retrieved 2025-10-08, from https://doi.org/10.1785/BSSA0870051288 doi: 10.1785/BSSA0870051288

Ellsworth, W. L., & Beroza, G. C. (1995). Seismic evidence for an earthquake nucleation phase. *Science*, *268*(5212), 851-855. Retrieved from https://www.science.org/doi/abs/10.1126/science.268.5212.851 doi: 10.1126/science.268.5212.851

Freund, L. B. (1998). *Dynamic fracture mechanics*. Cambridge university press.

Fryer, B., Garagash, D., Lebihain, M., & Passelègue, F. (2026). Foreshock-induced slip transients set mainshock nucleation timing. *Nature*, 1–6.

Fryer, B., Lebihain, M., Noël, C., Paglialunga, F., & Passelègue, F. (2024). The effect of stress barriers on unconventional-singularity-driven frictional rupture. *Journal of the Mechanics and Physics of Solids*, *193*, 105876. Retrieved from https://www.sciencedirect.com/science/article/pii/S0022509624003429 doi: https://doi.org/10.1016/j.jmps.2024.105876

Gori, M., Rubino, V., Rosakis, A. J., & Lapusta, N. (2021). Dynamic rupture initiation and propagation in a fluid-injection laboratory setup with diagnostics across multiple temporal scales. *Proceedings of the National Academy of Sciences*, *118*(51), e2023433118. Retrieved from https://www.pnas.org/doi/abs/10.1073/pnas.2023433118 doi: 10.1073/pnas.2023433118

Hayes, G. P. (2017). The finite, kinematic rupture properties of great-sized earthquakes since 1990. *Earth and Planetary Science Letters*, *468*, 94-100. Retrieved from https://www.sciencedirect.com/science/article/pii/S0012821X17301826 doi: https://doi.org/10.1016/j.epsl.2017.04.003

Husseini, M. I., Jovanovich, D. B., Randall, M. J., & Freund, L. B. (1975, 11). The fracture energy of earthquakes. *Geophysical Journal International*, *43*(2), 367-385. Retrieved from https://doi.org/10.1111/j.1365-246X.1975.tb00640.x doi: 10.1111/j.1365-246X.1975.tb00640.x

Ide, S. (2019). Frequent observations of identical onsets of large and small earthquakes. *Nature*, *573*(7772), 112–116. Retrieved from https://doi.org/10.1038/s41586-019-1508-5 doi: 10.1038/s41586-019-1508-5

Kammer, D. S., Radiguet, M., Ampuero, J.-P., & Molinari, J.-F. (2015). Linear elastic fracture mechanics predicts the propagation distance of frictional slip. *Tribology letters*, *57*(3), 23.

Kaneko, Y., Nielsen, S. B., & Carpenter, B. M. (2016). The onset of laboratory earthquakes explained by nucleating rupture on a rate-and-state fault. *Journal of Geophysical Research: Solid Earth*, *121*(8), 6071-6091. Retrieved from https://agupubs.onlinelibrary.wiley.com/doi/abs/10.1002/2016JB013143 doi: https://doi.org/10.1002/2016JB013143

Ke, C.-Y., McLaskey, G. C., & Kammer, D. S. (2018). Rupture termination in laboratory-generated earthquakes. *Geophysical Research Letters*, *45*(23), 12–784.

Kiss, A., Spagnuolo, E., Cornelio, C., Aretusini, S., Longobardi, V., Cocco, M., ... Colombelli, S. (2026). *Observations of laboratory earthquake rupture: implications for earthquake early warning.* (EGU General Assembly 2026, Vienna, Austria, 3–8 May 2026, EGU26-17668, https://doi.org/10.5194/egusphere-egu26-17668)

Latour, S., Passelègue, F., Paglialunga, F., Noël, C., & Ampuero, J.-P. (2024). What happens when two ruptures collide? *Geophysical Research Letters*, *51*(20), e2024GL110835. Retrieved from https://agupubs.onlinelibrary.wiley.com/doi/abs/10.1029/2024GL110835 (e2024GL110835 2024GL110835) doi: https://doi.org/10.1029/2024GL110835

Latour, S., Schubnel, A., Nielsen, S., Madariaga, R., & Vinciguerra, S. (2013). Characterization of nucleation during laboratory earthquakes. *Geophysical Research Letters*, *40*(19), 5064–5069. Retrieved 2026-04-05, from https://onlinelibrary.wiley.com/doi/abs/10.1002/grl.50974 doi: 10.1002/grl.50974

Longobardi, V., Colombelli, S., & Zollo, A. (2025, November). The deterministic behaviour of earthquake rupture beginning. *Communications Earth & Environment*, *6*(1), 883. Retrieved 2026-04-10, from https://www.nature.com/articles/s43247-025-02814-z (Publisher: Nature Publishing Group) doi: 10.1038/s43247-025-02814-z

McLaskey, G. C. (2019). Earthquake initiation from laboratory observations and implications for foreshocks. *Journal of Geophysical Research: Solid Earth*, *124*(12), 12882-12904. Retrieved from https://agupubs.onlinelibrary.wiley.com/doi/abs/10.1029/2019JB018363 doi: https://doi.org/10.1029/2019JB018363

McLaskey, G. C., & Lockner, D. A. (2014). Preslip and cascade processes initiating laboratory stick slip. *Journal of Geophysical Research: Solid Earth*, *119*(8), 6323–6336. Retrieved 2026-04-10, from https://onlinelibrary.wiley.com/doi/abs/10.1002/2014JB011220 doi: 10.1002/2014JB011220

Meier, M.-A., Ampuero, J.-P., Cochran, E., & Page, M. (2020, 12). Apparent earthquake rupture predictability. *Geophysical Journal International*, *225*(1), 657-663. doi: 10.1093/gji/ggaa610

Meier, M.-A., Ampuero, J. P., & Heaton, T. H. (2017). The hidden simplicity of subduction megathrust earthquakes. *Science*, *357*(6357), 1277-1281. Retrieved from https://www.science.org/doi/abs/10.1126/science.aan5643 doi: 10.1126/science.aan5643

Meier, M.-A., Heaton, T., & Clinton, J. (2016). Evidence for universal earthquake rupture initiation behavior. *Geophysical Research Letters*, *43*(15), 7991–7996. Retrieved 2026-04-07, from https://onlinelibrary.wiley.com/doi/abs/10.1002/2016GL070081 doi: 10.1002/2016GL070081

Melgar, D., & Hayes, G. P. (2019, May). Characterizing large earthquakes before rupture is complete. *Science Advances*, *5*(5), eaav2032. Retrieved 2025-09-19, from https://www.science.org/doi/10.1126/sciadv.aav2032 (Publisher: American Association for the Advancement of Science) doi: 10.1126/sciadv.aav2032

Morad, D., Gvirtzman, S., Gil, Y., Fineberg, J., & Brodsky, E. E. (2025, September). Under what circumstances is the final size of a laboratory earthquake predictable at the onset of the P-wave? *Earth and Planetary Science Letters*, *665*, 119436. Retrieved 2025-09-19, from https://www.sciencedirect.com/science/article/pii/S0012821X25002353 doi: 10.1016/j.epsl.2025.119436

Münchmeyer, J., Leser, U., & Tilmann, F. (2022). A probabilistic view on rupture predictability: All earthquakes evolve similarly. *Geophysical Research Letters*, *49*(13), e2022GL098344. doi: https://doi.org/10.1029/2022GL098344

Nakatani, M., Kaneshima, S., & Fukao, Y. (2000). Size-dependent microearthquake initiation inferred from high-gain and low-noise observations at nikko district, japan. *Journal of Geophysical Research: Solid Earth*, *105*(B12), 28095-28109. Retrieved from `https://agupubs.onlinelibrary.wiley.com/doi/abs/10.1029/2000JB900255` doi: https://doi.org/10.1029/2000JB900255

Nielsen, S., Taddeucci, J., & Vinciguerra, S. (2010). Experimental observation of stick-slip instability fronts. *Geophysical Journal International*, *180*(2), 697–702. Retrieved 2026-04-05, from `https://academic.oup.com/gji/article-lookup/doi/10.1111/j.1365-246X.2009.04444.x` doi: 10.1111/j.1365-246X.2009.04444.x

Ohnaka, M. (2004). Rupture in the laboratory. *Science*, *303*(5665), 1788-1789. Retrieved from `https://www.science.org/doi/abs/10.1126/science.1095765` doi: 10.1126/science.1095765

Okubo, P. G., & Dieterich, J. H. (1984). Effects of physical fault properties on frictional instabilities produced on simulated faults. *Journal of Geophysical Research: Solid Earth*, *89*(B7), 5817-5827. Retrieved from `https://agupubs.onlinelibrary.wiley.com/doi/abs/10.1029/JB089iB07p05817` doi: https://doi.org/10.1029/JB089iB07p05817

Paglialunga, F., Ampuero, J. P., & Passelègue, F. (2026). Stress barriers and their impact on rupture propagation. *Journal of Geophysical Research: Solid Earth*, *131*(2), e2025JB032879. doi: https://doi.org/10.1029/2025JB032879

Pardo, S., Corbi, F., Guastamacchia, S., Mastella, G., Tinti, E., & Funiciello, F. (2026). *Can earthquake magnitude be predicted at rupture onset? insights from scaled seismotectonic models.* (EGU General Assembly 2026, Vienna, Austria, 3–8 May 2026, EGU26-12207, https://doi.org/10.5194/egusphere-egu26-12207)

Passelègue, F. X., Almakari, M., Dublanchet, P., Barras, F., Fortin, J., & Violay, M. (2020). Initial effective stress controls the nature of earthquakes. *Nature communications*, *11*(1), 5132.

Renou, J., Vallée, M., & Dublanchet, P. (2019). How does seismic rupture accelerate? observational insights from earthquake source time functions. *Journal of Geophysical Research: Solid Earth*, *124*(8), 8942-8952. Retrieved from `https://agupubs.onlinelibrary.wiley.com/doi/abs/10.1029/2019JB018045` doi: https://doi.org/10.1029/2019JB018045

Rosakis, A., Samudrala, O., & Coker, D. (1999, 06). Cracks faster than the shear wave speed. *Science (New York, N.Y.)*, *284*, 1337-40. doi: 10.1126/science.284.5418.1337

Rubin, A. M., & Ampuero, J.-P. (2005). Earthquake nucleation on (aging) rate and state faults. *Journal of Geophysical Research: Solid Earth*, *110*(B11).

Tada, H., Paris, P., & Irwin, G. (2000). *The stress analysis of cracks handbook, third edition.* ASME Press.

Trugman, D. T., Page, M. T., Minson, S. E., & Cochran, E. S. (2019). Peak ground displacement saturates exactly when expected: Implications for earthquake early warning. *Journal of Geophysical Research: Solid Earth*, *124*(5), 4642–4653. Retrieved 2026-04-07, from `https://onlinelibrary.wiley.com/doi/abs/10.1029/2018JB017093` doi: 10.1029/2018JB017093

Vallée, M., & Douet, V. (2016). A new database of source time functions (STFs) extracted from the SCARDEC method. *Physics of the Earth and Planetary Interiors*, *257*, 149–157. Retrieved from `https://www.sciencedirect.com/science/article/pii/S0031920116300735` doi: https://doi.org/10.1016/j.pepi.2016.05.012

Wang, J., Ma, Q., Tao, D., Xie, Q., & Ren, X. (2022, 08). Weak predictability of rupture growth evidenced by p waves: Implications for earthquake early warning. *Bulletin of the Seismological Society of America*, *112*(5), 2653-2667. Retrieved from `https://doi.org/10.1785/0120210316` doi: 10.1785/0120210316

Ye, L., Lay, T., Kanamori, H., & Rivera, L. (2016). Rupture characteristics of major and great (mw7.0) megathrust earthquakes from 1990 to 2015: 1. source parameter scaling relationships. *Journal of Geophysical Research: Solid Earth*, *121*(2), 826-844. Retrieved from https://agupubs.onlinelibrary.wiley.com/doi/abs/10.1002/2015JB012426 doi: https://doi.org/10.1002/2015JB012426

Zeng, S., Guo, R., Zou, X., Dai, K., Liao, B., Xu, J., ... Sun, H. (2025). Whether and when large earthquake magnitudes can be determined from rupture onsets. *Journal of Geophysical Research: Machine Learning and Computation*, *2*(4), e2025JH000801. Retrieved from https://agupubs.onlinelibrary.wiley.com/doi/abs/10.1029/2025JH000801 doi: https://doi.org/10.1029/2025JH000801

Zollo, A., Lancieri, M., & Nielsen, S. (2006). Earthquake magnitude estimation from peak amplitudes of very early seismic signals on strong motion records. *Geophysical Research Letters*, *33*(23). Retrieved from https://agupubs.onlinelibrary.wiley.com/doi/abs/10.1029/2006GL027795 doi: https://doi.org/10.1029/2006GL027795